

Three-level Haldane-like model on a dice optical latticeT. Andrijauskas,¹ E. Anisimovas,¹ M. Račiūnas,¹ A. Mekys,¹ V. Kudriašov,¹ I. B. Spielman,^{2,3} and G. Juzeliūnas¹¹*Institute of Theoretical Physics and Astronomy, Vilnius University, A. Goštauto 12, Vilnius LT-01108, Lithuania*²*Joint Quantum Institute, University of Maryland, College Park, Maryland 20742-4111, 20742, USA*³*National Institute of Standards and Technology, Gaithersburg, Maryland 20899, USA*

(Received 5 May 2015; published 21 September 2015)

We consider ultracold atoms in a two-dimensional optical lattice of the dice geometry in a tight-binding regime. The atoms experience a laser-assisted tunneling between the nearest neighbor sites of the dice lattice accompanied by the momentum recoil. This allows one to engineer staggered synthetic magnetic fluxes over plaquettes, and thus pave a way towards the realization of topologically nontrivial band structures. In such a lattice the real-valued next-nearest neighbor transitions are not needed to reach a topological regime. Yet, such transitions can increase a variety of the obtained topological phases. The dice lattice represents a triangular Bravais lattice with a three-site basis consisting of a hub site connected to two rim sites. As a consequence, the dice lattice supports three energy bands. From this point of view, our model can be interpreted as a generalization of the paradigmatic Haldane model which is reproduced if one of the two rim sublattices is eliminated. We demonstrate that the proposed upgrade of the Haldane model creates a significant added value, including an easy access to topological semimetal phases relying only on the nearest neighbor coupling, as well as enhanced topological band structures featuring Chern numbers higher than one leading to physics beyond the usual quantum Hall effect. The numerical investigation is supported and complemented by an analytical scheme based on the study of singularities in the Berry connection.

DOI: [10.1103/PhysRevA.92.033617](https://doi.org/10.1103/PhysRevA.92.033617)

PACS number(s): 67.85.-d, 37.10.Jk, 73.43.-f

I. INTRODUCTION

Optical lattices have firmly established themselves as a modern and versatile tool to study fundamental physics in a clean environment with various physical parameters being under experimentalist's control and often extensively tunable [1–3]. One is typically interested in implementing a paradigmatic Hamiltonian that clearly demonstrates a particular phenomenon or an effect. A list of recent successes features, to mention just a few examples, realization of the Harper-Hofstadter [4–6] and Haldane models [7], direct observation and control of the Dirac points [8], creation of artificial magnetic fluxes via lattice shaking [9] and reproduction of models of magnetism [10], and engineering of a spin-dependent optical lattice resulting from a combination of Raman coupling and radio-frequency magnetic fields [11].

In particular, access to topological band structures is of enormous interest [12–14]. The presence of the topological order is signaled by a nonzero Chern index reflecting a nonvanishing integral of the Berry curvature over the entire two-dimensional Brillouin zone. A topological band supported by a spatially periodic optical lattice acts as a model of a Landau level. The unique band structure consisting of a ladder of Landau levels defines an apparent insulator with current-carrying edge states and has traditionally been associated with the presence of an external magnetic field. In cold-atom setups, however, the topological character becomes an intrinsic property of the band and is not necessarily associated with the presence of a physical magnetic field [14,15]. Synthetic fluxes piercing the lattice plaquettes may be imparted by the lattice shaking [9,14,16–18], laser-assisted tunneling [14,19–21] or using synthetic dimensions [22].

Many of the breakthroughs mentioned in the introductory paragraph can be classified as mimicking or reproduction of phenomena known from the condensed matter physics.

However, significant contributions from cold-atom systems to *extending* the known physics should also be recognized [1,2,14,21,23]. Perhaps the most obvious examples relate to the construction of topological bands with the values of the Chern index greater than one [24–30], which is a central topic of the present paper. The properties of such a band is not a direct sum of the properties of several Landau levels, and reach beyond the traditional (integer or fractional) quantum Hall physics [31,32].

Indeed, the study of bands with higher Chern numbers has been particularly relevant in connection to the so-called fractional Chern insulators [33–35]. Although many-body interactions, which play the central role in these studies, are beyond the scope of the present contribution, we stress that many insights into the nature of the fractional topological states were obtained from somewhat artificial lattice constructs often involving many layers [25] or distant-neighbor hoppings [26,27,36]. Ongoing efforts [37–40] are also based on the Harper-Hofstadter model that in principle supports subbands of arbitrarily high Chern numbers. Here, one also has to defy rather stringent requirements posed by large magnetic unit cells, low particle densities, and a large number of subbands implying small topological band gaps [40]. In the present paper we focus on exploring the potential offered by relatively *simple* and thus more realistic lattice models. We construct a generalization of the Haldane model [41–45] by coupling three rather than two triangular sublattices. In this way, the honeycomb lattice featured in the Haldane model is upgraded to the dice lattice [46–51] which supports a three-band model with a clean access to interesting topological configurations, such as bands characterized by the Chern number equal to 2. In the dice-lattice model it is just a complex valued nearest-neighbor (NN) coupling that is sufficient to generate a *staggered* synthetic magnetic flux and reach nontrivial setups

including a topological semimetal phase. On the other hand, for spatially periodic hexagonal lattices, nontrivial phases cannot be reached just by having the complex-valued nearest-neighbor coupling, one should add a real-valued next-neighbor coupling [42–44]. Note that the dice lattice affected by a *uniform* magnetic flux was used to demonstrate a novel and intriguing mechanism of localization of wave packets in Aharonov-Bohm cages [52–54].

The paper is structured as follows. In Sec. II, we introduce the lattice geometry and derive the 3×3 momentum-space Hamiltonian encapsulating the physics. Then, Sec. III describes the obtained results starting from phases obtained in the presence of NN couplings alone and proceeding to more complex configurations requiring next-nearest neighbor (NNN) transitions. We conclude with a brief summarizing Sec. V.

II. THE MODEL

A. Lattice geometry

We consider a dice lattice, which consists of three triangular sublattices. One of them is called a *hub* sublattice. It is coupled to other two *rim* sublattices, that in turn are not coupled with each other. Let us denote the hub sublattice by B and the rim sublattices by A and C. The vectors that connect the nearest lattice sites are (Fig. 1)

$$\delta_1 = \frac{a}{2}(e_x + \sqrt{3}e_y), \quad \delta_2 = \frac{a}{2}(e_x - \sqrt{3}e_y), \quad \delta_3 = -ae_x, \quad (1)$$

where a is the distance between two such sites. The elementary lattice vectors,

$$\mathbf{a}_1 = a(3e_x + \sqrt{3}e_y)/2, \quad \mathbf{a}_2 = a(3e_x - \sqrt{3}e_y)/2, \quad (2)$$

define a rhombic elementary cell. The set of lattice vectors $\mathbf{r}_n = n_1\mathbf{a}_1 + n_2\mathbf{a}_2$ (with integers n_1 and n_2) span the hub sublattice B (Bravais lattice). The two rim sublattices are defined in the following way. The first rim sublattice A is shifted from the hub sublattice B by the vector δ_1 in such a way that sublattices A and B alone make a honeycomb lattice.

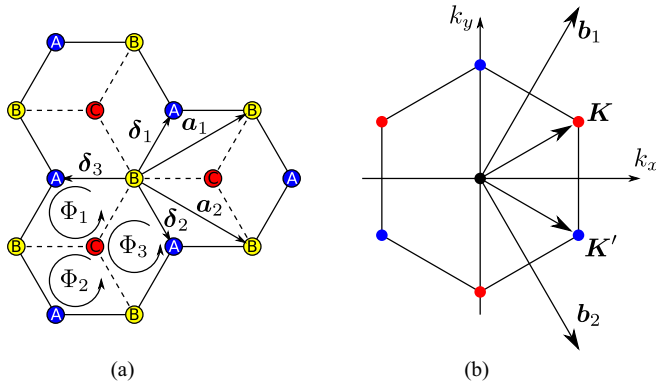


FIG. 1. (Color online) (a) Dice lattice. The blue, green, and red sites correspond to three different triangular sublattices A, B, and C. Solid lines show couplings between the sites A and B. Dashed lines show couplings between the sites B and C. The primitive lattice vectors are \mathbf{a}_1 and \mathbf{a}_2 . Nearest sites are connected with the vectors δ_1 , δ_2 , and δ_3 . (b) Hexagonal first Brillouin zone of the reciprocal lattice defined by the primitive reciprocal lattice vectors \mathbf{b}_1 and \mathbf{b}_2 . Two inequivalent corners are at the points \mathbf{K} (red) and \mathbf{K}' (blue).

The second rim sublattice C is shifted to the opposite direction by $-\delta_1$ (see Fig. 1). Let us introduce a set of vectors, that span all the lattice sites:

$$\mathbf{r}_{n,s} = \mathbf{r}_n + s\delta_1. \quad (3)$$

Here the index $s = 0, \pm 1$ labels the three sublattices. The sites of the hub sublattice ($s = 0$) coincide with the lattice vectors: $\mathbf{r}_{n,0} = \mathbf{r}_n$. The sites of the rim sublattices A and C shifted by $\pm\delta_1$, i.e., $\mathbf{r}_{n,+1} = \mathbf{r}_n + \delta_1$ and $\mathbf{r}_{n,-1} = \mathbf{r}_n - \delta_1$.

It is convenient to introduce an additional lattice vector $\mathbf{a}_3 = \mathbf{a}_1 - \mathbf{a}_2$. The set of the three lattice vectors \mathbf{a}_i ($i = 1, 2, 3$) together with the opposite vectors $-\mathbf{a}_i$ connect all next-nearest lattice sites, and can be related to δ_i as $\mathbf{a}_1 = \delta_1 - \delta_3$, $\mathbf{a}_2 = \delta_2 - \delta_3$, and $\mathbf{a}_3 = \delta_1 - \delta_2$.

The basic reciprocal lattice vectors,

$$\mathbf{b}_1 = \frac{2\pi}{3a}(e_x + \sqrt{3}e_y), \quad \mathbf{b}_2 = \frac{2\pi}{3a}(e_x - \sqrt{3}e_y), \quad (4)$$

are orthogonal to the lattice vectors, $\mathbf{a}_i \cdot \mathbf{a}_j = 2\pi\delta_{ij}$, $i, j = 1, 2$. The first Brillouin zone is hexagonal with two inequivalent corners \mathbf{K} and \mathbf{K}' positioned at $\mathbf{K} = (2\mathbf{b}_1 + \mathbf{b}_2)/3$ and $\mathbf{K}' = (\mathbf{b}_1 + 2\mathbf{b}_2)/3$. In terms of the Cartesian coordinates these points are given by

$$\mathbf{K} = \frac{2\pi}{9a}(3e_x + \sqrt{3}e_y), \quad \mathbf{K}' = \frac{2\pi}{9a}(3e_x - \sqrt{3}e_y), \quad (5)$$

as one can see in Fig. 1.

B. Tight-binding model

We shall make use of the tight-binding model in which the single-particle states $|\mathbf{r}_{n,s}\rangle$ represent the Wannier-type wave functions localized at each lattice site $\mathbf{r}_{n,s}$, with $s = 0, \pm 1$ being the sublattice index. In the language of the second quantization these single-particle states read $|\mathbf{r}_{n,s}\rangle = c^\dagger(\mathbf{r}_{n,s})|\text{vac}\rangle$, where $|\text{vac}\rangle$ is the Fock vacuum state, $c^\dagger(\mathbf{r}_{n,s})$ and $c(\mathbf{r}_{n,s})$ being the creation and annihilation operators of an atom in the corresponding localized state.

The full Hamiltonian of the system consist of three terms,

$$H = H_1 + H_2 + H_3. \quad (6)$$

The first term H_1 describes the laser-assisted tunneling [14,18–21,42,44,55] of atoms between the sites of the hub sublattice B ($s = 0$) and its nearest neighboring sites that belong to the rim sublattices A and C with $s = \pm 1$:

$$H_1 = \sum_n \sum_{s=\pm 1} J^{(s)} \sum_{i=1}^3 e^{i\mathbf{p}_s \cdot (\mathbf{r}_n + s\delta_i/2)} c^\dagger(\mathbf{r}_n) c(\mathbf{r}_n + s\delta_i) + \text{H.c.}, \quad (7)$$

where $J^{(s)}$ are the coupling amplitudes. Such generalization of dice optical lattice with two different hopping parameters $J^{(+)}$ and $J^{(-)}$ is already discussed in Ref. [56]. The laser-assisted tunneling is accompanied by the transfer of the recoil momentum \mathbf{p}_s with $s = \pm 1$, to be labeled simply by $\mathbf{p}_\pm \equiv \mathbf{p}_{\pm 1}$. In the present situation \mathbf{p}_+ can generally differ from \mathbf{p}_- because the transitions between the different sublattices can be induced by different lasers. Note that the nearest neighbor hopping alone is sufficient to generate fluxes through rhombic plaquettes,

$$\Phi_i = \pm(\mathbf{p}_+ - \mathbf{p}_-) \cdot \mathbf{a}_i/2, \quad (8)$$

with \mathbf{a}_i representing a diagonal vector of the plaquette in question. Yet the magnetic flux over the whole hexagonal plaquette remains zero.

The second term H_2 takes into account the tunneling between the next-nearest neighboring sites belonging to the same sublattice with $s = 0, \pm 1$:

$$H_2 = \sum_{\mathbf{n}} \sum_{s=0,\pm 1} J_2^{(s)} \sum_{i=1}^3 c^\dagger(\mathbf{r}_{\mathbf{n},s}) c(\mathbf{r}_{\mathbf{n},s} + \mathbf{a}_i) + \text{H.c.} \quad (9)$$

This term describes the usual (not laser-assisted) hopping transitions between nearest sites in each of the three triangular sublattices, and $J_2^{(s)}$ with $s = 0, \pm 1$ are the corresponding matrix elements for the tunneling between the atoms belonging to the s th sublattice.

The third term H_3 describes the energy mismatch for the particles populating the different sublattices:

$$H_3 = \sum_{\mathbf{n}} \sum_{s=0,\pm 1} \varepsilon_s c^\dagger(\mathbf{r}_{\mathbf{n},s}) c(\mathbf{r}_{\mathbf{n},s}). \quad (10)$$

The on-site energies ε_s are the diagonal matrix elements of the Hamiltonian in the basis of the Wannier states. Without a loss of generality we can take the on-site energy of the hub

sublattice B to be zero: $\varepsilon_0 = 0$. The on-site energies of other *rim* sublattices are to be labeled as $\varepsilon_{\pm 1} \equiv \varepsilon_{\pm}$.

Since the first term H_1 involves complex phase factors that depend on the elementary cell number \mathbf{n} , the full Hamiltonian H is not translationally invariant. Yet, we will transform the annihilation operators according to $c(\mathbf{r}_{\mathbf{n},0}) \rightarrow c(\mathbf{r}_{\mathbf{n},0})$ and $c(\mathbf{r}_{\mathbf{n},s}) \rightarrow c(\mathbf{r}_{\mathbf{n},s}) \exp(-i\mathbf{p}_s \cdot \mathbf{r}_{\mathbf{n}})$ with $s = \pm 1$, and perform the corresponding transformation for the creation operators. This gauge transformation makes the full Hamiltonian (6) translationally invariant.

Transition to the reciprocal space is carried out by introducing new operators,

$$c_s(\mathbf{k}) = \frac{1}{\sqrt{N}} \sum_{\mathbf{r}_n} c(\mathbf{r}_{\mathbf{n},s}) e^{-i\mathbf{k} \cdot \mathbf{r}_n}, \quad (11)$$

$$c(\mathbf{r}_{\mathbf{n},s}) = \frac{1}{\sqrt{N}} \sum_{\mathbf{k}} c_s(\mathbf{k}) e^{i\mathbf{k} \cdot \mathbf{r}_n},$$

together with the Hermitian conjugated creation operators $c_s^\dagger(\mathbf{k})$. Here N is a number of elementary cells in the quantization area, and the vectors $\mathbf{r}_n = \mathbf{r}_{\mathbf{n},0}$ (defined in Sec. II A) are located at the sites of the hub lattice. In terms of the new operators the Hamiltonian (6) splits into its \mathbf{k} components:

$$H = \sum_{\mathbf{k}} H(\mathbf{k}), \quad H(\mathbf{k}) = \begin{bmatrix} c_+^\dagger(\mathbf{k}) & c_0^\dagger(\mathbf{k}) & c_-^\dagger(\mathbf{k}) \end{bmatrix} \mathcal{H}(\mathbf{k}) \begin{bmatrix} c_+(\mathbf{k}) \\ c_0(\mathbf{k}) \\ c_-(\mathbf{k}) \end{bmatrix}, \quad (12)$$

where $\mathcal{H}(\mathbf{k})$ is a 3×3 matrix:

$$\mathcal{H}(\mathbf{k}) = \begin{bmatrix} \varepsilon_+ + 2J_2^{(+)} f(\mathbf{k} - \mathbf{p}_+) & J^{(+)} g(\mathbf{k} - \mathbf{p}_+/2) & 0 \\ J^{(+)} g^*(\mathbf{k} - \mathbf{p}_+/2) & 2J_2^{(0)} f(\mathbf{k}) & J^{(-)} g(\mathbf{k} - \mathbf{p}_-/2) \\ 0 & J^{(-)} g^*(\mathbf{k} - \mathbf{p}_-/2) & \varepsilon_- + 2J_2^{(-)} f(\mathbf{k} - \mathbf{p}_-) \end{bmatrix}. \quad (13)$$

Here we also added an extra phase factor to the transformed operators $c_s(\mathbf{k}) \rightarrow c_s(\mathbf{k}) e^{i\mathbf{p}_s \cdot \mathbf{s}\delta_1/2}$. The functions,

$$f(\mathbf{k}) = \sum_{i=1}^3 \cos(\mathbf{k} \cdot \mathbf{a}_i), \quad g(\mathbf{k}) = e^{i\mathbf{k} \cdot \delta_1} \sum_{i=1}^3 e^{-i\mathbf{k} \cdot \delta_i}, \quad (14)$$

entering Eq. (13) are translationally symmetric in the reciprocal space,

$$f(\mathbf{k} + \mathbf{G}) = f(\mathbf{k}), \quad g(\mathbf{k} + \mathbf{G}) = g(\mathbf{k}), \quad (15)$$

where $\mathbf{G} = n_1 \mathbf{b}_1 + n_2 \mathbf{b}_2$ is a reciprocal lattice vector, n_1 and n_2 being integers. Consequently the matrix Hamiltonian $\mathcal{H}(\mathbf{k})$ is also fully translationally invariant in the reciprocal space $\mathcal{H}(\mathbf{k}) = \mathcal{H}(\mathbf{k} + \mathbf{G})$. Note that Berry curvature in general depends on the choice of Fourier transformation (11), while the corresponding Chern number does not [57,58]. Furthermore, the functions $f(\mathbf{k})$ and $g(\mathbf{k})$ obey the following reflection properties,

$$f(\mathbf{k}) = f(-\mathbf{k}), \quad g(\mathbf{k}) = g^*(-\mathbf{k}). \quad (16)$$

All this helps to consider various symmetries of the matrix Hamiltonian (13).

III. PHASES OF NONINTERACTING FERMIONS

A. Chern numbers and symmetries of the system

Since the momentum-space Hamiltonian (13) represents a three-level system, there are three energy bands characterized by energies $E_n(\mathbf{k})$, with $n = 1, 2, 3$. Each energy band has a Chern number c_n to be defined in Eq. (17). We also identify two possible band gaps. The first band gap Δ_{12} measures the energy between the first ($n = 1$) and second ($n = 2$) bands, the second band gap Δ_{23} corresponding to the energy between the second ($n = 2$) and the third ($n = 3$) bands.

The Chern number c_n for the n th band is defined in terms of a surface integral of a Berry curvature over the first Brillouin zone (FBZ) [14,59]:

$$c_n = -\frac{1}{2\pi} \int_{\text{FBZ}} d^2k F_n(\mathbf{k}). \quad (17)$$

The Berry curvature $F_n(\mathbf{k})$ can be expressed in terms of the eigenvectors $|u_{n,\mathbf{k}}\rangle$ of the reciprocal space Hamiltonian (13)

as

$$F_n(\mathbf{k}) = i \left(\frac{\partial}{\partial k_x} \langle u_{n,\mathbf{k}} | \right) \left(\frac{\partial}{\partial k_y} | u_{n,\mathbf{k}} \rangle \right) - i \left(\frac{\partial}{\partial k_y} \langle u_{n,\mathbf{k}} | \right) \left(\frac{\partial}{\partial k_x} | u_{n,\mathbf{k}} \rangle \right). \quad (18)$$

It is well defined as long the eigenenergies $E_n(\mathbf{k})$ are not degenerate for any fixed value of \mathbf{k} . Therefore the Chern number c_n can be ascribed to the n th band if the latter does not touch any other bands. If the Fermi energy is situated in a band gap, the Chern number is directly related to Hall conductivity due to chiral edge states of the occupied bands [60] via

$$\mathcal{H}(\mathbf{k}) = \begin{bmatrix} \varepsilon + 2J_2 f(\mathbf{k} - \mathbf{p}) & Jg(\mathbf{k} - \mathbf{p}/2) & 0 \\ Jg^*(\mathbf{k} - \mathbf{p}/2) & 2J_2 f(\mathbf{k}) & Jg(\mathbf{k} + \mathbf{p}/2) \\ 0 & Jg^*(\mathbf{k} + \mathbf{p}/2) & -\varepsilon + 2J_2 f(\mathbf{k} + \mathbf{p}) \end{bmatrix}. \quad (19)$$

This form of the Hamiltonian exhibits some symmetries. The first symmetry involves inversion of the on-site energies $\varepsilon \rightarrow -\varepsilon$ followed by the unitary transformation that changes the first row with the third one (i.e., interchanges the *rim* sublattices A and C), as well as the momentum inversion $\mathbf{k} \rightarrow -\mathbf{k}$. Using the reflection properties of the functions f and g given by Eq. (16), one arrives at the same Hamiltonian (19). The second symmetry is $J \rightarrow -J$, which is a simple gauge transformation. Using these two symmetries we see that the change $J_2 \rightarrow -J_2$ gives $\mathcal{H}(\mathbf{k}) \rightarrow -\mathcal{H}(\mathbf{k})$. To sum up, all the three mentioned symmetries are ($\varepsilon \rightarrow -\varepsilon, \mathcal{H} \rightarrow \mathcal{H}$), ($J \rightarrow -J, \mathcal{H} \rightarrow \mathcal{H}$), and ($J_2 \rightarrow -J_2, \mathcal{H} \rightarrow -\mathcal{H}$).

B. Numerical analysis

In this subsection, we numerically study the Chern phases of noninteracting fermions. In order to present dependence of the Chern number on the parameters ε , J , J_2 , and \mathbf{p} we adopt a similar presentation of the phase diagram scheme as in Ref. [44]. We choose the energy unit to be the nearest-neighbor tunneling amplitude J . For the recoil momentum \mathbf{p} , we express the p_x component in the units of K_x and the component p_y in the units of K_y , where \mathbf{K} is one of the FBZ corners, defined in Eq. (5). In all the phase diagrams we present the dependence of the Chern number $c_n = c_n(p_x, p_y)$ on the components of the recoil momentum \mathbf{p} using different colors for each possible values of c_n . The areas corresponding to a topologically trivial phase with a zero Chern number are shown in green ($c_n = 0$). On the other hand, the areas corresponding to nontrivial Chern phases are shown in yellow ($c_n = 1$), red ($c_n = 2$), cyan ($c_n = -1$), and blue ($c_n = -2$). Additionally we display Chern number labels in all the presented phase diagrams.

First we characterize topological properties of the band structure if there is no next-nearest neighbor coupling ($J_2=0$). In Fig. 2 we show the Chern number phase diagrams for $\varepsilon = J$. One can identify regions where the Chern numbers are $\{c_1, c_2, c_3\} = \{0, 0, 0\}$, $\{-1, 2, -1\}$, and $\{1, -2, 1\}$. In the first type of the regions (green color) we have topologically trivial

$\sigma_{xy} = -e^2 c_n / \hbar$ [61–63]. For numerical calculation we make use of the discretized version of the Berry curvature (18) described in Ref. [64].

For both *rim* sublattices A and C, we set on-site energies of to be symmetrically shifted away from the zero point $\varepsilon_+ = -\varepsilon_- = \varepsilon$. We also take the tunneling amplitudes to be equal $J^{(+)} = J^{(-)} = J$, $J_2^{(+)} = J_2^{(0)} = J_2^{(-)} = J_2$ and assume the recoil momenta to be opposite $\mathbf{p}_+ = -\mathbf{p}_- = \mathbf{p}$ for both *rim* sublattices A and C. The choice of opposite recoil momenta ensures the maximum flux, because the magnetic flux through a rhombic plaquette Φ_i given by Eq. (8) is proportional to the difference of these vectors. Under these conditions, the matrix representation of the \mathbf{k} -space Hamiltonian becomes

regions. In other regions there are nonzero Chern numbers with band gaps $\Delta_{12} = \Delta_{23} = 0$. Analysis of the band structure in these regions shows that the bands do not overlap and touch indirectly. Thus by filling the first one or the first two bands we arrive at semimetallic phase with nonzero Hall conductivity. The typical spectrum of such a nontrivial semimetallic case is presented in Fig. 6. The size of the nontrivial regions in the \mathbf{p} plane depends on the mismatch ε of the on-site energies of A and C sublattices. By increasing ε from zero these regions immediately appear around the points $\mathbf{p} = \mathbf{K}$ and become larger in size. For about $\varepsilon \approx J$ these regions have the largest area as presented in Fig. 2 for $\varepsilon = J$. For even larger values of ε the nontrivial regions shrink back to the points \mathbf{K} and finally we are left only with the trivial phase $\{0, 0, 0\}$ everywhere. The analytical treatment, presented in Sec. IV gives the value of

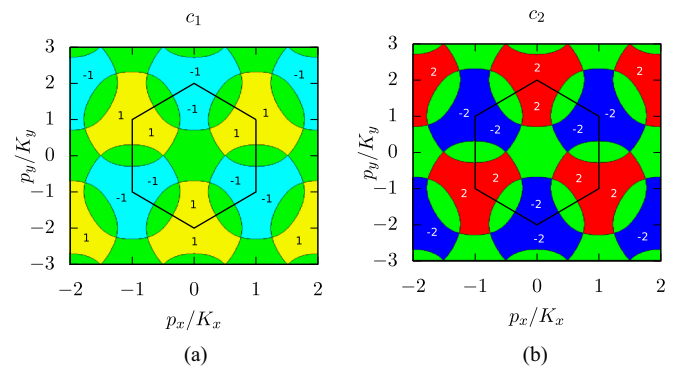


FIG. 2. (Color online) Chern number dependence on the recoil momentum \mathbf{p} in the case $\varepsilon = J$ and $J_2 = 0$. (a) The phase diagram of the lowest band Chern number c_1 . (b) The corresponding phase diagram for the middle band. Since the sum of Chern numbers over all three bands is zero, the third band gives the same phase diagram as the first one ($c_1 = c_3$). The green regions correspond to the Chern number zero. The yellow, red, cyan, and blue regions correspond to the Chern numbers 1, 2, -1, and -2, respectively. Nonzero Chern numbers are also displayed as labels. The hexagon represents the FBZ in the \mathbf{p} plane.

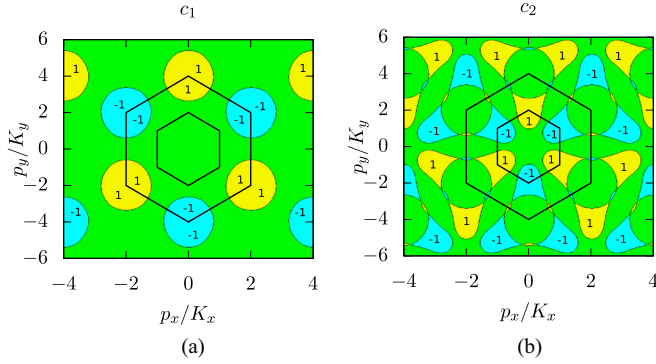


FIG. 3. (Color online) Chern number dependence on the recoil momentum \mathbf{p} in the case $\varepsilon = 2J$ and $J_2 = 0.3J$. (a) The Chern number c_1 of the lowest band; (b) the Chern number c_2 of the middle band. For the third band (not shown here) we have $c_3 = -(c_1 + c_2)$. The green, yellow, red, cyan, and blue regions correspond to the Chern numbers 0, 1, 2, -1, and -2, respectively. Nonzero Chern numbers are also displayed as labels. A smaller hexagon shows the FBZ corresponding to the case $J_2 = 0$. Since the introduction of nonzero J_2 changes the periodicity of the \mathbf{p} dependence, we also show a bigger hexagon, which is now the FBZ in the \mathbf{p} plane.

$\varepsilon = \frac{3\sqrt{2}}{2}J$ for which the semimetal regions completely disappear. For $J_2 = 0$ there are no other types of phases than the trivial and semimetallic discussed above. Nonzero band gaps appear only in the regions of trivial phase.

For the case $J_2 = 0$, the change $\mathbf{p} \rightarrow \mathbf{p} + \mathbf{G}$, where \mathbf{G} is the reciprocal lattice vector, corresponds to a gauge transformation. Thus there is a symmetry ($\mathbf{p} \rightarrow \mathbf{p} + \mathbf{G}, \mathcal{H} \rightarrow \mathcal{H}$). In the phase diagram (Fig. 2) we also show the FBZ in the \mathbf{p} plane, which is a hexagon with two inequivalent corners positioned at points \mathbf{K} and \mathbf{K}' .

Now let us analyze effects of the nonzero next-nearest neighbor coupling. For this we set $J_2 = 0.3J$ and $\varepsilon = 2J$. The phase diagrams of the Chern numbers are presented in Fig. 3. We can see regions with the Chern numbers corresponding to trivial phases $\{0,0,0\}$ and phases $\{0, \pm 1, \mp 1\}$ and $\{\pm 1, 0, \mp 1\}$. In the latter two types of regions we can find points corresponding to nonzero band gaps $\Delta_{12} > 0$ and/or $\Delta_{23} > 0$ (Fig. 4). This shows that there exist topological Chern insulating phases. For example, at the point $\mathbf{p} = \mathbf{K}$, we

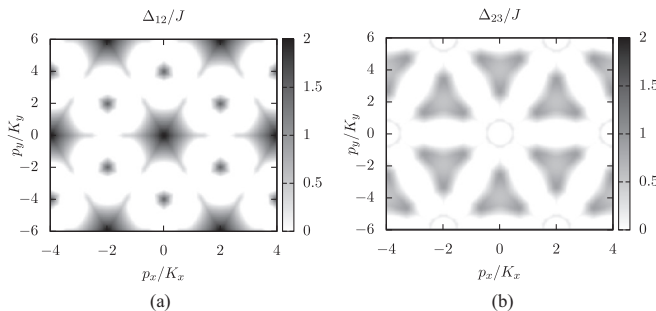


FIG. 4. Dependence of the band gap on the recoil momentum \mathbf{p} in the case where $\varepsilon = 2J$ and $J_2 = 0.3J$. (a) The band gap Δ_{12} between the first and second bands. (b) The band gap Δ_{23} between the second and third bands.

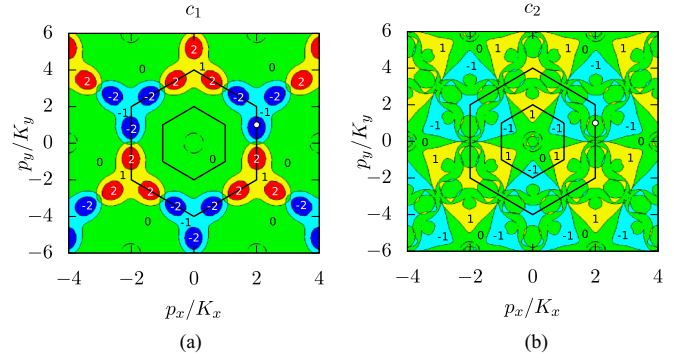


FIG. 5. (Color online) Chern number dependence on the recoil momentum in the case $\varepsilon = 0.5J$ and $J_2 = 0.5J$. (a) Chern number c_1 of the lowest band. (b) Chern number c_2 of the middle band. The color scheme and labeling are the same as in Figs. 2 and 3. The white point is $\mathbf{p} = (2K_x, K_y)$ where the Chern numbers are $c_1 = -2$, $c_2 = 0$, and c_3 (see the spectrum in Fig. 6).

have the Chern numbers $\{0, -1, 1\}$, the band gap between the middle and highest bands being $\Delta_{23} \approx 0.26J$. Band widths in this case are about $3J$. By positioning the Fermi energy in the gap between the second and third bands one arrives at the Chern insulating phase. Another interesting point is $\mathbf{p} = 2\mathbf{K}$, which gives the Chern numbers $\{-1, 0, 1\}$, the band gaps $\Delta_{12} \approx 1.55J$ and $\Delta_{23} \approx 0.54J$, and the band widths of about $2J$. The bottom and top bands have nonzero Chern numbers, while it is zero for the middle band. Depending on the filling there are two types of topologically nontrivial phases. If the Fermi energy is positioned in one of the band gaps, we get a topological insulating phase. If the Fermi energy is situated within a band, the band is partially filled and supports the Chern metal phase. The discussed types of Chern number distributions over the bands are typical when J_2 is nonzero and smaller than J and ε .

In the case of nonzero NNN coupling J_2 the translation symmetry in the recoil momentum \mathbf{p} is smaller than in the case of zero NNN couplings: One has to shift the momentum by $2\mathbf{G}$ rather than \mathbf{G} . In the phase diagram presented in Fig. 3 we show this by extending the FBZ, which is now a bigger hexagon.

There are more types of Chern phases when the coupling J_2 is larger than in the previous discussion and comparable to the on-site energy ε . For $\varepsilon = J_2 = 0.5J$ we find insulating phases with Chern numbers $\{\pm 1, \pm 1, \mp 2\}$ and metallic phases with Chern numbers $\{\pm 2, 0, \mp 2\}$ (Fig. 5). For example, in the point $\mathbf{p} = 2\mathbf{K}$ we get Chern numbers $c_1 = c_2 = -1$ and $c_3 = 2$ with band gaps $\Delta_{12} \approx 0.61J$ and $\Delta_{23} \approx 0.54J$. The width of the lower two bands are around $3J$, while the band width of the highest band is about $1.5J$. Another interesting point is $\mathbf{p} = (2K_x, K_y)$ where the Chern numbers are $c_1 = -2$, $c_2 = 0$, and $c_3 = 2$ (white point in Fig. 5). The bulk spectrum in this point is given in Fig. 6. Note that there is a gap $\Delta_{13} \approx 1.35J$ between the lowest and highest bands. In this gap there is a middle band with a zero Chern number. By setting the Fermi energy in this gap one gets the Chern metallic phase with the Chern number $c_1 = -2$.

To summarize the numeric analysis for $J_2 \neq 0$, the typical nontrivial Chern number distributions over the

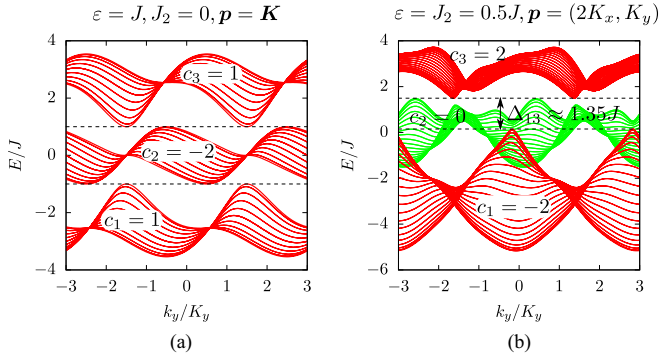


FIG. 6. (Color online) Bulk lattice spectrum projected along k_y for a number of different k_x values in the range $-K_x \leq k_x \leq K_x$. (a) The spectrum for the recoil momentum $\mathbf{p} = \mathbf{K}$ in the absence of the NNN coupling ($J_2 = 0$) and for $\varepsilon = J$ corresponding to the parameters used in Fig. 2. In that case there is no energy gap in the spectrum, but different energy bands do not directly touch each other. A topological semimetal phase is formed if the atoms fill the first energy band or the first two bands. (b) The spectrum for the recoil momentum $\mathbf{p} = (2K_x, K_y)$ in the case where $\varepsilon = 0.5J$ and $J_2 = 0.5J$ corresponding to the phase diagram shown in Fig. 5. Now there are two bands with nonzero Chern numbers ± 2 separated by a quasigap $\Delta_{13} \approx 1.35J$ containing a middle band with a zero Chern number.

bands are $\{0, \pm 1, \mp 1\}$, $\{\pm 1, \mp 1, 0\}$, $\{\pm 1, 0, \mp 1\}$, $\{\pm 1, \pm 1, \mp 2\}$, $\{\pm 2, \mp 1, \mp 1\}$, and $\{\pm 2, 0, \mp 2\}$. One can also find the case $\{\pm 1, \mp 2, \pm 1\}$, which is typical for $J_2 = 0$. For smaller J_2 compared to J and ε , one usually gets Chern numbers up to 1 in modulus. For larger Chern numbers (up to 2 in modulus), one needs to make the NNN-hopping J_2 be comparable to the on-site energy mismatch ε .

IV. ANALYTICAL CHERN NUMBER CALCULATION

Analytic Chern number calculation is based on integration of a Berry connection around each singularity point. The Berry connection of the n th band is defined as [14,59]

$$\mathbf{A}_n(\mathbf{k}) = i \langle u_{k,n} | \nabla_{\mathbf{k}} | u_{k,n} \rangle, \quad (20)$$

where $|u_{k,n}\rangle$ denotes the n th eigenvector of the matrix (13). One can express the Berry curvature (18) as the z component of the curl $\mathbf{B}_n = \nabla \times \mathbf{A}_n$, namely $F_n(\mathbf{k}) = \mathbf{e}_z \cdot \mathbf{B}_n$. Using the Stoke's theorem we change the integral featured in Eq. (17) over the FBZ to a contour integral around the FBZ,

$$\begin{aligned} & \frac{1}{2\pi} \int_{\text{FBZ}} d^2k F_n(\mathbf{k}) \\ & \rightarrow \frac{1}{2\pi} \oint_{\text{FBZ}} d\mathbf{k} \cdot \mathbf{A}_n - \frac{1}{2\pi} \sum \oint_{\text{singul}} d\mathbf{k} \cdot \mathbf{A}_n, \end{aligned}$$

where the last term excludes any contribution due to unphysical gauge-dependent singular points of the Berry connection [44,65,66]. Since the \mathbf{k} -space Hamiltonian $H(\mathbf{k})$, given by Eqs. (13) or (19), and its eigenstates are periodic in the FBZ, \mathbf{A}_n is also periodic. Thus the contour integral around the FBZ (the first term on the right-hand side of the above equation) is zero. Consequently the Chern number (17) can

be calculated by integrating \mathbf{A}_n around each excluded singular point [44]:

$$c_n = \frac{1}{2\pi} \sum \oint_{\text{singul}} d\mathbf{k} \cdot \mathbf{A}_n, \quad (21)$$

where the sum is over all singular points in the FBZ.

Let us summarize our analytical results, details being presented in the Appendix. For the case where the recoil momentum coincides with the inverse lattice vector ($\mathbf{p} = \mathbf{G}$) we always have trivial phase with all three Chern numbers equal to zero. For the semimetal case (Fig. 2) with no NNN hopping and $\mathbf{p} = \mathbf{K}$ we find two phases, depending on the mismatch ε of the on-site energies. If $\varepsilon < \varepsilon_0 = \frac{3\sqrt{2}}{2}J$, we get Chern semimetal phase with Chern numbers $\{1, -2, 1\}$. If $\varepsilon > \varepsilon_0$, we get a trivial phase $\{0, 0, 0\}$. In this way at larger mismatch between the on-site energies the topological phenomena disappear. This is in agreement with the numerical calculation presented in the previous section.

It is possible to apply this method for other values of the recoil momenta \mathbf{p} and for a general nonsymmetric case with the NNN hoppings. In such calculations one needs to diagonalize the matrices of the size at most 2×2 . Yet generally ordering of the eigenvalues might be a quite involved task, especially if they depend on more than one parameter.

V. CONCLUDING REMARKS

In conclusion, we have considered a two-dimensional dice lattice operating in a tight-binding regime. The laser-assisted nearest neighbor transitions are accompanied by the momentum recoils. This allows one to engineer staggered synthetic magnetic fluxes and thus facilitates realization of topologically nontrivial band structures. Real valued next-nearest neighbor transitions—although not necessary in principle to reach the topological regime—may also be present and contribute to the richness of the obtained topological phases. The considered dice lattice represents a triangular Bravais lattice with a three-site basis consisting of a hub site connected to two rim sites, providing three energy bands. Thus our model can be interpreted as a generalization of the paradigmatic Haldane model which is reproduced if one of the two rim sublattices is eliminated. We have demonstrated that the proposed upgrade of the Haldane model creates a significant added value such as (i) an easy access to topological semimetal phases relying on only the nearest neighbor coupling and (ii) enhanced topological band structures featuring Chern numbers higher than one and thus providing access to physics beyond the usual quantum Hall effect. The numerical analysis has been supported by an analytical scheme based on the study of singularities in the Berry connection.

ACKNOWLEDGMENTS

This research was supported by the Research Council of Lithuania (Grant No. MIP-082/2012). I.B.S. was partially supported by the ARO's atomtronics MURI, the AFOSR's Quantum Matter MURI, NIST, and the NSF through the PFC at the JQI.

APPENDIX: DETAILS ON ANALYTICAL CHERN NUMBER CALCULATION

1. Momentum space Hamiltonian and its eigenstates

Let us establish a general structure of the eigenstates for the matrix Hamiltonian $\mathcal{H}(\mathbf{k})$, Eq. (19). For this we introduce a basis of our three-level system $|s\rangle$, with $s = 0, \pm 1$, and rewrite the matrix Hamiltonian in the state-vector notation as

$$\mathcal{H}(\mathbf{k}) = \sum_{s=0,\pm 1} |s\rangle d_s(\mathbf{k}) \langle s| + \sum_{s=\pm 1} (|s\rangle g_s(\mathbf{k}) e^{i s \alpha_s(\mathbf{k})} \langle 0| + \text{H.c.}), \quad (\text{A1})$$

where $d_s(\mathbf{k})$ stands for the diagonal matrix elements:

$$d_s(\mathbf{k}) = s\varepsilon + 2J_2 f(\mathbf{k} - s\mathbf{p}). \quad (\text{A2})$$

The off-diagonal matrix elements,

$$Jg(\mathbf{k} \mp \mathbf{p}/2) = g_{\pm}(\mathbf{k}) e^{i\alpha_{\pm}(\mathbf{k})}, \quad (\text{A3})$$

have been represented in terms of their amplitudes $g_{\pm 1}(\mathbf{k}) \equiv g_{\pm}(\mathbf{k})$ and phases $\alpha_{\pm 1}(\mathbf{k}) \equiv \alpha_{\pm}(\mathbf{k})$.

Since there is no coupling between the A and C sublattices, one can perform a \mathbf{k} -dependent unitary transformation eliminating the phase factors,

$$|s\rangle \rightarrow |s, \mathbf{k}\rangle = |s\rangle e^{i s \alpha_s(\mathbf{k})}, \quad s = \pm 1,$$

and leave the basis vector $|0\rangle$ unchanged ($|0\rangle = |0, \mathbf{k}\rangle$). In the new basis the Hamiltonian (A1) is characterized by real and symmetric matrix elements. Its eigenvectors can be cast in terms of these vectors with real coefficients $C_{n,s}(\mathbf{k})$:

$$|u_{\mathbf{k},n}\rangle = \sum_{s=0,\pm 1} C_{n,s}(\mathbf{k}) |s, \mathbf{k}\rangle \equiv \sum_{s=0,\pm 1} |s\rangle C_{n,s}(\mathbf{k}) e^{i s \alpha_s(\mathbf{k})}. \quad (\text{A4})$$

Combining Eqs. (20) and (A4), one arrives at the following expression for the Berry connection:

$$A_n(\mathbf{k}) = - \sum_{s=\pm 1} s C_{n,s}^2(\mathbf{k}) \nabla_{\mathbf{k}} \alpha_s(\mathbf{k}). \quad (\text{A5})$$

This result together with Eq. (21) will be subsequently used in finding the Chern numbers.

2. Determination of the Chern numbers: General

To determine the Chern number given by (21), one needs to study a behavior of the vector potential at its singular points. Singularities of the vector potential can emerge at the points where the phase of the coupling matrix element $g_{\pm}(\mathbf{k}) e^{i\alpha_{\pm}(\mathbf{k})}$ given by Eq. (A3) is undefined. This happens if the function $g(\mathbf{k} - \mathbf{p}_{\pm}/2)$ goes to zero. The function $g(\mathbf{k})$ given by Eq. (14) is zero at the corners of the FBZ, namely at two inequivalent points \mathbf{K} and \mathbf{K}' . Thus there are two pairs of points,

$$\mathbf{K}_{\pm} = \pm \mathbf{p}/2 + \mathbf{K}, \quad \mathbf{K}'_{\pm} = \pm \mathbf{p}/2 + \mathbf{K}', \quad (\text{A6})$$

at which the function $g(\mathbf{k} \mp \mathbf{p}/2)$ goes to zero and its phase $\alpha_{\pm}(\mathbf{k})$ is undefined. Let us determine the coupling matrix element $g_{\pm}(\mathbf{k}) e^{i\alpha_{\pm}(\mathbf{k})}$ in a vicinity of these points. Combining Eqs. (14) and (A3), the amplitude and phase of the coupling element reads up to the first order in the displacement vector

\mathbf{q} , i.e., for $qa \ll 1$ with $q = |\mathbf{q}|$:

$$g_{\pm}(\mathbf{K}_{\pm} + \mathbf{q}) \approx \frac{3}{2} qaJ, \quad \alpha_{\pm}(\mathbf{K}_{\pm} + \mathbf{q}) \approx \frac{\pi}{3} - \varphi, \quad (\text{A7})$$

$$g_{\pm}(\mathbf{K}'_{\pm} + \mathbf{q}) \approx \frac{3}{2} qaJ, \quad \alpha_{\pm}(\mathbf{K}'_{\pm} + \mathbf{q}) \approx -\frac{\pi}{3} + \varphi, \quad (\text{A8})$$

where φ is a phase of the complex number $q_x + iq_y = qe^{i\varphi}$. Integrating over a small circle centered at $\mathbf{q} = 0$ surrounding each singular point of the phase, one finds

$$\oint_{|\mathbf{q}| \rightarrow 0} d\mathbf{q} \cdot \nabla_{\mathbf{q}} \alpha_{\pm}(\mathbf{K}_{\pm} + \mathbf{q}) = -2\pi,$$

$$\oint_{|\mathbf{q}| \rightarrow 0} d\mathbf{q} \cdot \nabla_{\mathbf{q}} \alpha_{\pm}(\mathbf{K}'_{\pm} + \mathbf{q}) = 2\pi,$$

where the signs are different due to the opposite phases in Eqs. (A7) and (A8). These equations together with Eqs. (21) and (A5) provide the following result for the Chern number:

$$c_n = \sum_{s=\pm 1} s [C_{n,s}^2(\mathbf{K}_s) - C_{n,s}^2(\mathbf{K}'_s)], \quad (\text{A9})$$

with $\mathbf{K}_{\pm 1} \equiv \mathbf{K}_{\pm}$ and $\mathbf{K}'_{\pm 1} \equiv \mathbf{K}'_{\pm}$. Therefore to find the Chern number one needs to determine the coefficients $C_{n,s}$ entering the state vector at the points \mathbf{K}_{\pm} and \mathbf{K}'_{\pm} . If $C_{n,\pm}^2 = 1$, the corresponding singular point contributes to the Chern number of the n th band. In the following we shall analyze two different situations.

3. Determination of the Chern numbers: Specific cases

Since the Hamiltonian $\mathcal{H}(\mathbf{k})$ given by Eqs. (19) or (A1) has a symmetry ($\varepsilon \rightarrow -\varepsilon, \mathcal{H} \rightarrow \mathcal{H}$), we consider only the case where $\varepsilon > 0$.

a. The case where $\mathbf{p} = \mathbf{G}$

Suppose first that the difference in the recoil momenta coincides with the inverse lattice vector $\mathbf{p} = \mathbf{G}$. In that case the coupling completely vanishes both for $\mathbf{k} = \mathbf{K}_{\pm}$ and also for $\mathbf{k} = \mathbf{K}'_{\pm}$. At these points $g(\mathbf{k} - \mathbf{p}/2) = g(\mathbf{k} + \mathbf{p}/2) = 0$, so all the states $|s\rangle$ ($s = 0, \pm 1$) are decoupled, and thus the eigenstates are the bare states $|s\rangle$. The corresponding eigenenergies of the matrix Hamiltonian $\mathcal{H}(\mathbf{k})$, Eq. (A1), coincide with its diagonal elements $d_s(\mathbf{k})$ for $\mathbf{k} = \mathbf{K}_{\pm}$ and $\mathbf{k} = \mathbf{K}'_{\pm}$. Since $\mathbf{p} = \mathbf{G}$, one has $f(\mathbf{k} - \mathbf{p}) = f(\mathbf{k}) = f(\mathbf{k} + \mathbf{p})$, giving $d_s(\mathbf{k}) = s\varepsilon + 2J_2 f(\mathbf{k})$. Therefore the eigenstates are ordered in the same manner $d_{+1}(\mathbf{k}) > d_0(\mathbf{k}) > d_{-1}(\mathbf{k})$ both for $\mathbf{k} = \mathbf{K}_{\pm}$ and also $\mathbf{k} = \mathbf{K}'_{\pm}$, giving $C_{n,s}^2(\mathbf{K}_s) = C_{n,s}^2(\mathbf{K}'_s)$ with $s = \pm 1$. As a result, the Chern number given by Eq. (A9) is identically equal to zero, and the system does not exhibit any topologically nontrivial phases. This is because for $\mathbf{p} = \mathbf{G}$ the flux over the rhombic plaquettes $\Phi_i = \pm \mathbf{p} \cdot \mathbf{a}_i$ is zero (modulo 2π), and there is no breaking of the time-reversal symmetry.

b. The case where $\mathbf{p} = \mathbf{K}$

As another illustration we pick the recoil momentum $\mathbf{p} = \mathbf{K}$ and take $J_2 = 0$. In that case the Chern numbers have been numerically found to be $c_1 = 1$, $c_2 = -2$, and $c_3 = 1$ (see Fig. 2). By taking $\mathbf{p} = \mathbf{K}$ the phase singularities of the coupling elements $g(\mathbf{k} \mp \mathbf{p}/2)$ emerge at the points

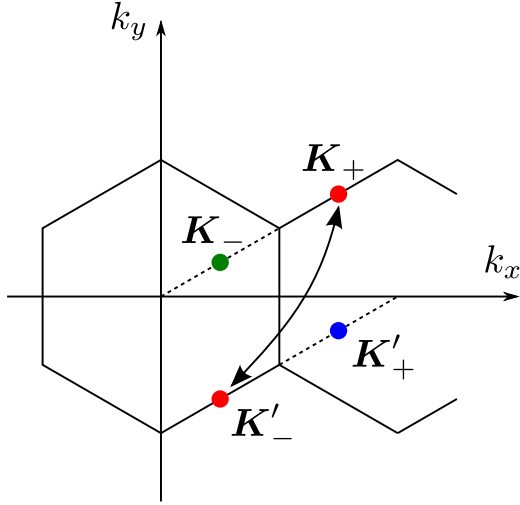


FIG. 7. (Color online) The phase singularity points \mathbf{K}_\pm and \mathbf{K}'_\pm of the coupling matrix elements $g(\mathbf{k} \mp \mathbf{p}/2)$ for $\mathbf{p} = \mathbf{K}$. The points \mathbf{K}_+ and \mathbf{K}'_- are equivalent. They are shown by red dots connected with a double arrow.

$\mathbf{K}_\pm = \pm \mathbf{K}/2 + \mathbf{K}$ and $\mathbf{K}'_\pm = \pm \mathbf{K}/2 + \mathbf{K}'$, as one can see in Fig. 7. Furthermore, the point $\mathbf{k} = \mathbf{K}_+$ is equivalent to the point $\mathbf{k} = \mathbf{K}'_-$. For the latter two points we have $g(\mathbf{k} - \mathbf{p}/2) = g(\mathbf{k} + \mathbf{p}/2) = 0$, so there are no coupling matrix elements. Since $J_2 = 0$, the Hamiltonian (A1) at these points is, simply,

$$\mathcal{H}(\mathbf{K}_+) = \mathcal{H}(\mathbf{K}'_-) = \varepsilon \sum_{s=\pm 1} s|s\rangle\langle s|, \quad (\text{A10})$$

so the diagonal energies entering the Hamiltonian (A1) are $d_s(\mathbf{k}) = s\varepsilon$.

Eigenvalues, ordered from the lowest to the highest, are $E_1(\mathbf{K}_+) = E_1(\mathbf{K}'_-) = -\varepsilon$, $E_2(\mathbf{K}_+) = E_2(\mathbf{K}'_-) = 0$, and $E_3(\mathbf{K}_+) = E_3(\mathbf{K}'_-) = \varepsilon$. There is no degeneracy for $\varepsilon > 0$ and the coefficients $C_{n,+}(\mathbf{K}_+)$ and $C_{n,-}(\mathbf{K}'_-)$ do not change if one increases ε . The only nonzero coefficients contributing to the Chern numbers read

$$C_{3,+}(\mathbf{K}_+) = C_{1,-}(\mathbf{K}'_-) = 1. \quad (\text{A11})$$

For the point $\mathbf{k} = \mathbf{K}_-$ the nondiagonal matrix elements of (A1) are $Jg(\mathbf{k} + \mathbf{p}/2) = 0$ and $Jg(\mathbf{k} - \mathbf{p}/2) = 3J$. Similarly for the point $\mathbf{k} = \mathbf{K}'_+$ these elements are $Jg(\mathbf{k} - \mathbf{p}/2) = 0$ and $Jg(\mathbf{k} + \mathbf{p}/2) = 3J$. Thus the Hamiltonian (A1) at these points is

$$H(\mathbf{K}_-) = \varepsilon \sum_{s=\pm 1} s|s\rangle\langle s| + 3J(|0\rangle\langle +| + |+\rangle\langle 0|), \quad (\text{A12})$$

$$H(\mathbf{K}'_+) = \varepsilon \sum_{s=\pm 1} s|s\rangle\langle s| + 3J(|0\rangle\langle -| + |-\rangle\langle 0|). \quad (\text{A13})$$

Eigenvalues of the $H(\mathbf{K}_-)$ are $E^{(0)}(\mathbf{K}_-) = -\varepsilon$ and $E^{(\pm)}(\mathbf{K}_-) = \frac{1}{2}(\varepsilon \pm \sqrt{\varepsilon^2 + 36J^2})$, and those of $H(\mathbf{K}'_+)$ are $E^{(0)}(\mathbf{K}'_+) = \varepsilon$ and $E^{(\pm)}(\mathbf{K}'_+) = \frac{1}{2}(-\varepsilon \pm \sqrt{\varepsilon^2 + 36J^2})$. They

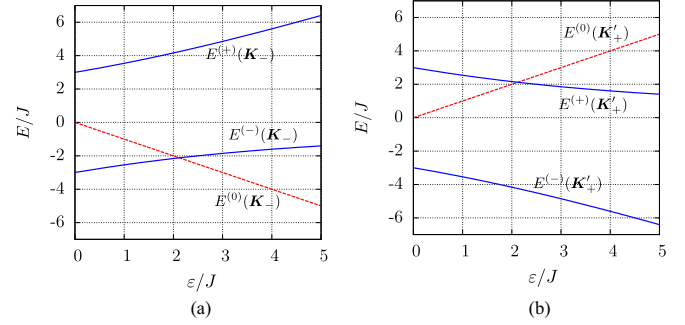


FIG. 8. (Color online) Dependence of eigenvalues of the Hamiltonian $H(\mathbf{k})$ on the on-site energy ε for $\mathbf{p} = \mathbf{K}$ in the absence of the next-nearest neighbor coupling. The eigenvalue $E^{(0)}$ is plotted in red dashed lines to distinguish it from the other eigenvalues $E^{(\pm)}$. (a) Eigenvalues at the point $\mathbf{k} = \mathbf{K}_-$. (b) Eigenvalues at the point $\mathbf{k} = \mathbf{K}'_+$. The eigenvalue crossing point $\varepsilon = \frac{3\sqrt{2}}{2}J \equiv \varepsilon_0$ corresponds to a transition from a topological semimetal phase on the left to a trivial phase on the right.

are plotted in Fig. 8. For $\varepsilon = \frac{3\sqrt{2}}{2}J \equiv \varepsilon_0$ there are degeneracies $E^{(0)}(\mathbf{K}_-) = E^{(-)}(\mathbf{K}_-) = -\varepsilon_0$ and $E^{(0)}(\mathbf{K}'_+) = E^{(+)}(\mathbf{K}'_+) = \varepsilon_0$. The eigenvalues change their order at the crossing point $\varepsilon = \varepsilon_0$, as one can see in Fig. 8.

Let us first consider the case $0 < \varepsilon < \varepsilon_0$. The eigenvalues of $H(\mathbf{K}_-)$ are in the increasing order: $E_1(\mathbf{K}_-) = E^{(-)}(\mathbf{K}_-)$, $E_2(\mathbf{K}_-) = E^{(0)}(\mathbf{K}_-)$, and $E_3(\mathbf{K}_-) = E^{(+)}(\mathbf{K}_-)$. On the other hand, coefficients required for the Chern number calculation are $C_{1,-}(\mathbf{K}_-) = 0$, $C_{2,-}(\mathbf{K}_-) = 1$, and $C_{3,-}(\mathbf{K}_-) = 0$. Similarly $H(\mathbf{K}'_+)$ gives the eigenvalues $E_1(\mathbf{K}'_+) = E^{(-)}(\mathbf{K}'_+)$, $E_2(\mathbf{K}'_+) = E^{(0)}(\mathbf{K}'_+)$, and $E_3(\mathbf{K}'_+) = E^{(+)}(\mathbf{K}'_+)$ and the coefficients $C_{1,+}(\mathbf{K}'_+) = 0$, $C_{2,+}(\mathbf{K}'_+) = 1$ and $C_{3,+}(\mathbf{K}'_+) = 0$. Combining this result together with (A11) we collect four nonzero coefficients: $C_{3,+}(\mathbf{K}_+)$, $C_{1,-}(\mathbf{K}'_-)$, $C_{2,-}(\mathbf{K}_-)$, and $C_{2,+}(\mathbf{K}'_+)$. Substituting them into Eq. (A9), we get the Chern numbers for each energy band:

$$c_1 = C_{1,-}^2(\mathbf{K}'_-) = 1, \quad (\text{A14})$$

$$c_2 = -C_{2,+}^2(\mathbf{K}'_+) - C_{2,-}^2(\mathbf{K}_-) = -2, \quad (\text{A15})$$

$$c_3 = C_{3,+}^2(\mathbf{K}_+) = 1. \quad (\text{A16})$$

This result agrees with the numerical analysis presented in Fig. 2.

Now let us consider the case $\varepsilon > \varepsilon_0$. From Fig. 8 we see that the eigenvalues are reordered as $E_1(\mathbf{K}_-) \rightarrow E_2(\mathbf{K}_-)$, $E_2(\mathbf{K}'_+) \rightarrow E_3(\mathbf{K}'_+)$, so nonzero coefficients are $C_{3,+}(\mathbf{K}_+)$, $C_{1,-}(\mathbf{K}'_-)$, $C_{1,-}(\mathbf{K}_-)$, and $C_{3,+}(\mathbf{K}'_+)$. Using Eq. (A9), one can see that the Chern numbers of all bands are now zero:

$$c_1 = -C_{1,-}^2(\mathbf{K}_-) + C_{1,-}^2(\mathbf{K}'_-) = 0, \quad (\text{A17})$$

$$c_2 = 0, \quad (\text{A18})$$

$$c_3 = C_{3,+}^2(\mathbf{K}_+) - C_{3,+}^2(\mathbf{K}'_+) = 0. \quad (\text{A19})$$

Thus there is a topological phase transition at $\varepsilon = \frac{3\sqrt{2}}{2}J$ corresponding to the eigenvalue crossing in Fig. 8.

- [1] I. Bloch, J. Dalibard, and W. Zwerger, *Rev. Mod. Phys.* **80**, 885 (2008).
- [2] M. Lewenstein, A. Sanpera, V. Ahufinger, B. Damski, A. Sen(De), and U. Sen, *Adv. Phys.* **56**, 243 (2007).
- [3] P. Windpassinger and K. Sengstock, *Rep. Prog. Phys.* **76**, 086401 (2013).
- [4] M. Aidelsburger, M. Atala, M. Lohse, J. T. Barreiro, B. Paredes, and I. Bloch, *Phys. Rev. Lett.* **111**, 185301 (2013).
- [5] H. Miyake, G. A. Siviloglou, C. J. Kennedy, W. C. Burton, and W. Ketterle, *Phys. Rev. Lett.* **111**, 185302 (2013).
- [6] D. R. Hofstadter, *Phys. Rev. B* **14**, 2239 (1976).
- [7] G. Jotzu, M. Messer, R. Desbuquois, M. Lebrat, T. Uehlinger, D. Greif, and T. Esslinger, *Nature (London)* **515**, 237 (2014).
- [8] L. Tarruell, D. Greif, T. Uehlinger, G. Jotzu, and T. Esslinger, *Nature (London)* **483**, 302 (2012).
- [9] J. Struck, C. Ölschläger, M. Weinberg, P. Hauke, J. Simonet, A. Eckardt, M. Lewenstein, K. Sengstock, and P. Windpassinger, *Phys. Rev. Lett.* **108**, 225304 (2012).
- [10] J. Struck, M. Weinberg, C. Ölschläger, P. Windpassinger, J. Simonet, K. Sengstock, R. Höppner, P. Hauke, A. Eckardt, M. Lewenstein, and L. Mathey, *Nat. Phys.* **9**, 738 (2013).
- [11] K. Jiménez-García, L. J. LeBlanc, R. A. Williams, M. C. Beeler, A. R. Perry, and I. B. Spielman, *Phys. Rev. Lett.* **108**, 225303 (2012).
- [12] M. Z. Hasan and C. L. Kane, *Rev. Mod. Phys.* **82**, 3045 (2010).
- [13] X.-L. Qi and S.-C. Zhang, *Rev. Mod. Phys.* **83**, 1057 (2011).
- [14] N. Goldman, G. Juzeliūnas, P. Öhberg, and I. B. Spielman, *Rep. Prog. Phys.* **77**, 126401 (2014).
- [15] D. N. Sheng, Z.-C. Gu, K. Sun, and L. Sheng, *Nat. Commun.* **2**, 389 (2011).
- [16] A. Eckardt, C. Weiss, and M. Holthaus, *Phys. Rev. Lett.* **95**, 260404 (2005).
- [17] A. R. Kolovsky, *Europhys. Lett.* **93**, 20003 (2011).
- [18] N. Goldman and J. Dalibard, *Phys. Rev. X* **4**, 031027 (2014).
- [19] D. Jaksch and P. Zoller, *New J. Phys.* **5**, 56 (2003).
- [20] F. Gerbier and J. Dalibard, *New J. Phys.* **12**, 033007 (2010).
- [21] J. Dalibard, F. Gerbier, G. Juzeliūnas, and P. Öhberg, *Rev. Mod. Phys.* **83**, 1523 (2011).
- [22] A. Celi, P. Massignan, J. Ruseckas, N. Goldman, I. B. Spielman, G. Juzeliūnas, and M. Lewenstein, *Phys. Rev. Lett.* **112**, 043001 (2014).
- [23] T. Dubček, C. J. Kennedy, L. Lu, W. Ketterle, M. Soljačić, and H. Buljan, *Phys. Rev. Lett.* **114**, 225301 (2015).
- [24] Y.-F. Wang, Z.-C. Gu, C.-D. Gong, and D. N. Sheng, *Phys. Rev. Lett.* **107**, 146803 (2011).
- [25] Z. Liu, E. J. Bergholtz, H. Fan, and A. M. Läuchli, *Phys. Rev. Lett.* **109**, 186805 (2012).
- [26] S. Yang, Z.-C. Gu, K. Sun, and S. Das Sarma, *Phys. Rev. B* **86**, 241112 (2012).
- [27] Y.-F. Wang, H. Yao, C.-D. Gong, and D. N. Sheng, *Phys. Rev. B* **86**, 201101 (2012).
- [28] A. Sterdyniak, C. Repellin, B. A. Bernevig, and N. Regnault, *Phys. Rev. B* **87**, 205137 (2013).
- [29] F. Wang and Y. Ran, *Phys. Rev. B* **84**, 241103 (2011).
- [30] D. Sticlet, F. Piéchon, J.-N. Fuchs, P. Kalugin, and P. Simon, *Phys. Rev. B* **85**, 165456 (2012).
- [31] S. A. Parameswaran, R. Roy, and S. L. Sondhi, *C. R. Phys.* **14**, 816 (2013).
- [32] E. J. Bergholtz and Z. Liu, *Int. J. Mod. Phys. B* **27**, 1330017 (2013).
- [33] T. Neupert, L. Santos, C. Chamon, and C. Mudry, *Phys. Rev. Lett.* **106**, 236804 (2011).
- [34] N. Regnault and B. A. Bernevig, *Phys. Rev. X* **1**, 021014 (2011).
- [35] A. G. Grushin, A. Gómez-León, and T. Neupert, *Phys. Rev. Lett.* **112**, 156801 (2014).
- [36] D. Sticlet and F. Piéchon, *Phys. Rev. B* **87**, 115402 (2013).
- [37] A. Kol and N. Read, *Phys. Rev. B* **48**, 8890 (1993).
- [38] R. N. Palmer and D. Jaksch, *Phys. Rev. Lett.* **96**, 180407 (2006).
- [39] G. Möller and N. R. Cooper, *Phys. Rev. Lett.* **103**, 105303 (2009).
- [40] G. Moller and N. R. Cooper, [arXiv:1504.06623](https://arxiv.org/abs/1504.06623).
- [41] F. D. M. Haldane, *Phys. Rev. Lett.* **61**, 2015 (1988).
- [42] E. Alba, X. Fernandez-Gonzalvo, J. Mur-Petit, J. K. Pachos, and J. J. Garcia-Ripoll, *Phys. Rev. Lett.* **107**, 235301 (2011).
- [43] G. Juzeliūnas and I. B. Spielman, *Physics* **4**, 99 (2011).
- [44] N. Goldman, E. Anisimovas, F. Gerbier, P. Öhberg, I. B. Spielman, and G. Juzeliūnas, *New J. Phys.* **15**, 013025 (2013).
- [45] E. Anisimovas, F. Gerbier, T. Andrijauskas, and N. Goldman, *Phys. Rev. A* **89**, 013632 (2014).
- [46] B. Sutherland, *Phys. Rev. B* **34**, 5208 (1986).
- [47] D. Bercioux, D. F. Urban, H. Grabert, and W. Häusler, *Phys. Rev. A* **80**, 063603 (2009).
- [48] G. Möller and N. R. Cooper, *Phys. Rev. Lett.* **108**, 045306 (2012).
- [49] M. Rizzi, V. Cataudella, and R. Fazio, *Phys. Rev. B* **73**, 144511 (2006).
- [50] A. A. Burkov and E. Demler, *Phys. Rev. Lett.* **96**, 180406 (2006).
- [51] D. Bercioux, N. Goldman, and D. F. Urban, *Phys. Rev. A* **83**, 023609 (2011).
- [52] J. Vidal, R. Mosseri, and B. Douçot, *Phys. Rev. Lett.* **81**, 5888 (1998).
- [53] C. C. Abilio, P. Butaud, T. Fournier, B. Pannetier, J. Vidal, S. Tedesco, and B. Dalzotto, *Phys. Rev. Lett.* **83**, 5102 (1999).
- [54] J. L. Movilla and J. Planelles, *Phys. Rev. B* **84**, 195110 (2011).
- [55] J. Ruostekoski, G. V. Dunne, and J. Javanainen, *Phys. Rev. Lett.* **88**, 180401 (2002).
- [56] A. Raoux, M. Morigi, J.-N. Fuchs, F. Piéchon, and G. Montambaux, *Phys. Rev. Lett.* **112**, 026402 (2014).
- [57] T. S. Jackson, G. Möller, and R. Roy, [arXiv:1408.0843](https://arxiv.org/abs/1408.0843).
- [58] E. Dobardžić, M. Dimitrijević, and M. V. Milovanović, *Phys. Rev. B* **91**, 125424 (2015).
- [59] D. Xiao, M.-C. Chang, and Q. Niu, *Rev. Mod. Phys.* **82**, 1959 (2010).
- [60] Y. Hatsugai, *Phys. Rev. Lett.* **71**, 3697 (1993).
- [61] M. Kohmoto, *Ann. Phys.* **160**, 343 (1985).
- [62] M. Kohmoto, *Phys. Rev. B* **39**, 11943 (1989).
- [63] D. J. Thouless, M. Kohmoto, M. P. Nightingale, and M. den Nijs, *Phys. Rev. Lett.* **49**, 405 (1982).
- [64] T. Fukui, Y. Hatsugai, and H. Suzuki, *J. Phys. Soc. Jpn.* **74**, 1674 (2005).
- [65] Y. Hatsugai, *J. Phys. Soc. Jpn.* **74**, 1374 (2005).
- [66] M. Hafezi, A. S. Sørensen, M. D. Lukin, and E. Demler, *Europhys. Lett.* **81**, 10005 (2008).